

A Mathematical Model of Fluid Transport in an Accurate Reconstruction of Parotid Acinar Cells.

Elias Vera-Siguenza¹  · Nathan Pages¹
 · John Rugis¹ · David I. Yule² · James
Sneyd¹ 

Received: date / Accepted: date

Abstract Salivary gland acinar cells use the calcium (Ca^{2+}) ion as a signalling messenger to regulate a diverse range of intracellular processes, including the secretion of primary saliva. Although the underlying mechanisms responsible for saliva secretion are reasonably well understood, the precise role played by spatially heterogeneous intracellular Ca^{2+} signalling in these cells remains uncertain.

In this study we use a mathematical model, based on new and unpublished experimental data from parotid acinar cells (measured in excised lobules of mouse parotid gland), to investigate how the structure of the cell and the spatio-temporal properties of Ca^{2+} signalling influence the production of primary saliva. We combine a new Ca^{2+} signalling model (described in detail in a companion paper: Pages et al. (2018), submitted) with an existing secretion model (Vera-Siguenza E, et al., Bull Math Biol 80: 255–282, 2018. <https://doi.org/10.1007/s11538-017-0370-6>) and solve the resultant model in an anatomically-accurate three-dimensional cell.

Our study yields three principal results. Firstly, we show that spatial heterogeneities of Ca^{2+} concentration in either the apical or basal regions of the cell have no significant effect on the rate of primary saliva secretion. Secondly, in agreement with previous work (Palk L., et al., 2012, J. Theor. Biol. 305:45–53, <http://dx.doi.org/10.1016/j.jtbi.2012.04.009>) we show that the frequency of Ca^{2+} oscillation has no significant effect on the rate of primary saliva secretion, which is determined almost entirely by the mean (over time) of the apical and basal $[\text{Ca}^{2+}]$. Thirdly, it is possible to model the rate of primary saliva secretion as a quasi-steady state function of the cytosolic $[\text{Ca}^{2+}]$ averaged over the entire cell when modelling the flow rate is the only interest, thus ignoring all the dynamic complexity not only of the fluid secretion mechanism but also of the intracellular heterogeneity of $[\text{Ca}^{2+}]_i$.

¹Department of Mathematics, The University of Auckland, Level 2, Building 303, 38 Princes Street, Auckland CBD, New Zealand, E-mail: elias.siguenza@auckland.ac.nz

²University of Rochester Medical Center, School of Medicine and Dentistry, 601 Elmwood Ave, Box 711, Rochester NY, United States of America

Taken together, our results demonstrate that an accurate multiscale model of primary saliva secretion from a single acinar cell can be constructed by ignoring the vast majority of the spatial and temporal complexity of the underlying mechanisms.

Keywords Salivary Epithelia · Parotid Gland · Fluid Secretion · Plasma Membrane · Saliva · Ca^{2+} Signalling · Ca^{2+} Mathematical Modelling · Ion Channels

1 Introduction

In most mammals the majority of saliva is secreted by three principal pairs of exocrine glands: the parotid, the sub-mandibular, and the sub-lingual. Clusters of salivary epithelia, called acini, secrete a primary fluid into a collecting region called the acinar lumen. The collected secretion is low in potassium (K^+), but its sodium (Na^+) and chloride (Cl^-) concentrations are similar to those in plasma (Martin and Young, 1971). Along with evidence regarding the inhomogeneous distribution of plasma membrane (PM) transporters, channels and exchangers in water-transporting epithelia, these observations led to the construction of the currently accepted secretion model (Silva et al., 1977). In this model, basolateral PM mechanisms accumulate Cl^- to levels well above its electrochemical equilibrium. Following an increase in the intracellular concentration of calcium ($[\text{Ca}^{2+}]_i$), a Cl^- efflux through apical Ca^{2+} -dependent Cl^- channels generates a transepithelial osmotic gradient. Water follows this gradient by osmosis.

Cl^- uptake via basolateral $\text{Na}^+-\text{K}^+-2\text{Cl}^-$ cotransporters (*Nkcc1*) is the major driver of fluid secretion in acinar cells, and its inhibition causes an approximate 70% decrease in the rate of saliva secretion (Evans et al., 2000). The residual secretion is bicarbonate (HCO_3^-)-dependent and involves two Na^+/H^+ (*Nhe1*) paired $\text{Cl}^-/\text{HCO}_3^-$ anion exchangers: the anion exchanger 2 (*Ae2*) and the anion exchanger 4 (*Ae4*) (Melvin et al., 2005). However, recent studies by Peña-Münzenmayer et al. (2015) revealed that only the *Ae4* is relevant in the secretory process. Experiments on *Ae4* knockout mice exhibited a decreased gland fluid secretion ($\sim 30\%$ of the control fluid flow rate), whereas mice lacking *Ae2* expression displayed an unchanged secretion rate. Sigüenza et al. (2018) developed a mathematical model, based on Palk et al. (2010), that aimed to understand the mechanisms behind these results. The model supports the observations by Peña-Münzenmayer et al. (2015) and suggests that the *Ae4*'s cotransport of monovalent cations is likely to be important in establishing the osmotic gradient necessary for optimal transepithelial fluid movement.

The model of Sigüenza et al. (2018) assumes that $[\text{Ca}^{2+}]_i$ is a given function of time (for example, a given constant), not a dependent variable. Although this simplifies the computations, there is a great deal of evidence that Ca^{2+} spatio-temporal phenomena are involved in water transport (Foskett, 1990; Palk et al., 2012; Tanimura, 2009). In particular, it is well known that Ca^{2+} travels in waves from apical to basolateral regions of the cell (Foskett et al., 1991; Foskett and Melvin, 1989). These encode a large amount of signalling information that a constant, and homogeneous, $[\text{Ca}^{2+}]_i$ does not. Variations in wave amplitude, mean concentration, frequency, and also wave speed serve as potential modifiers of saliva secretion.

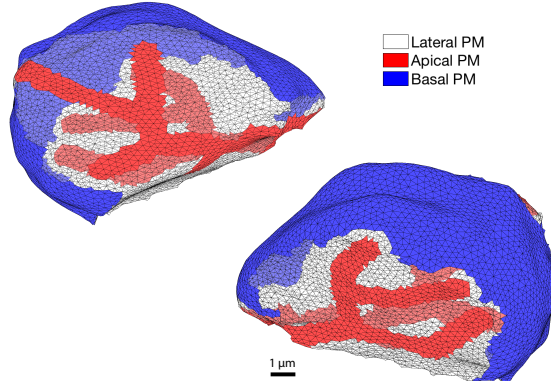


Fig. 1: A parotid acinar cell depicted by a tetrahedral mesh. Two images of the same cell are shown. The cell is rotated to exhibit the apical (red) and basal (blue) regions of the plasma membrane (PM). The non-coloured triangular faces represent its lateral portion. The image reflects the hallmark pyramidal-shape seen in several water secreting epithelia. Details of the mesh construction can be found in Pages et al. (2018).

In this study we investigate how the three-dimensional structure of a salivary acinar cell and the spatio-temporal heterogeneities of Ca^{2+} signalling affect transepithelial water transport. To do so, we use a partial differential equation model of Ca^{2+} signalling to drive fluid secretion on seven anatomically-accurate three-dimensional cells consisting of individual volumetric tetrahedral meshes. The details of the Ca^{2+} signalling model, and construction of the meshes, are presented in a companion paper by Pages et al (2018). Here we demonstrate that given physiologically accurate spatio-temporal Ca^{2+} responses to agonist-induced stimulation, each acinar cell will secrete primary saliva at the correct physiological rate. In addition, we show that the model reproduces critical experimental data, including the expected changes in cellular volume and the concentrations of the ionic species involved in fluid secretion such as Cl^- , Na^+ , K^+ , HCO_3^- and H^+ . We conclude with a brief discussion on how many of the complexities of a spatial Ca^{2+} signalling model are unnecessary in the modelling of primary secretion by these epithelia.

2 Experimental Data and Cell Reconstruction

The model presented in this study uses a mesh constructed by Pages et al. (2018), and described in detail there. Briefly, it is based on 31 confocal microscopy images of parotid gland epithelia at 1024 by 1024 pixels, with a resolution of $0.069 \mu\text{m}$ per pixel and a stack spacing of $0.8 \mu\text{m}$. These consist of fluorescent staining of the apical Ca^{2+} -dependent Cl^- channels, (*TMeM16a*), and NaK-ATPases as a way to visualise apical and basolateral plasma membranes of acinar cells. Using these data, a mesh was created of a cluster of seven cells where every cell touches at least one or more other cells. Here, we present in detail the results of our model applied to one of these cells (Fig. 1). Refer to the supporting material for the results in all seven cells.

The Ca^{2+} dynamics model is based on previously unpublished data from excised parotid gland lobules stimulated by 300 nM Carbachol (CCh), as described in Pages et al. (2018) and in Section 3.3.

3 Secretion Model

3.1 Assumptions

We use the mathematical model of primary secretion developed by [Sigüenza et al. \(2018\)](#). Here, the interstitial and luminal compartments are modelled as constant volume sub-domains. In particular, the interstitial space is assumed to be an infinite ionic bath (i.e., all its ionic concentrations are constant). Furthermore, with the exception of $[Ca^{2+}]_i$, the ionic species are assumed well-stirred at all times throughout the three compartments. This is because the intracellular diffusion of the ions involved in fluid secretion occurs relatively fast compared to the time scale in which water travels across the cell and its plasma membrane (from interstitium to lumen) ([Swietach et al., 2003](#)).

Saliva flow is initiated, from rest, by an agonist-induced $[Ca^{2+}]_i$ increase that causes the opening of apical Ca^{2+} -activated Cl^- channels (*TMem16a*) in order to establish a Cl^- efflux into the acinar lumen. This is maintained by a compensating K^+ current through the basolateral Ca^{2+} -activated K^+ channels (*BK/IK*), along with a paracellular cation current. Consequently, an osmotic gradient from the interstitium, through the cell, to the lumen is created, enabling the flow of water in the secretory direction (see Fig. 2). In our model the Ca^{2+} -activated Cl^- channels are restricted to the apical PM ([Young, 1968](#)), and the Ca^{2+} -activated K^+ channels are restricted to the basolateral PM. Although there is evidence for a limited number of Ca^{2+} -activated K^+ channels on the apical PM considerable uncertainty as to the relative distribution between apical and basolateral PM exists, so for simplicity we choose to avoid this question entirely ([Almássy et al., 2012](#)). This problem has been addressed in previous studies ([Almássy et al., 2018; Palk et al., 2010](#)). The distributions of all pumps, transporters, and exchangers in their respective PM portions are assumed to be homogeneous (see Fig. 2). As a consequence, the PM electric potentials, basolateral and apical alike, are also homogeneous. Finally, as a simplification, we do not include the basolateral anion exchanger 2 (*Ae2*). This is because the exchanger has been shown to be less important for fluid secretion ([Peña-Münzenmayer et al., 2015; Sigüenza et al., 2018](#)).

3.2 Equations

We introduce the subscripts, e , i , and l to denote, respectively, the interstitial, intracellular, and luminal compartments. The cellular PM fluxes are denoted by j , and each flux is represented by a sub-model based on experimental data (where possible) and/or previous models. To take the three-dimensional structure of the cell into account requires only a small modification from the previous model of [Sigüenza et al. \(2018\)](#). All the ions, with the exception of Ca^{2+} , which is treated in detail in a companion paper ([Pages et al., 2018](#)) are assumed to be spatially homogeneous. Thus, conservation gives, for Cl^- , say,

$$\frac{d([Cl^-]_{i\omega})}{dt} = \int_{\partial\Omega_b} \left(2j_{Nkcc1} + j_{Ae4} \right) dS - \int_{\partial\Omega_a} j_{Cl} dS,$$

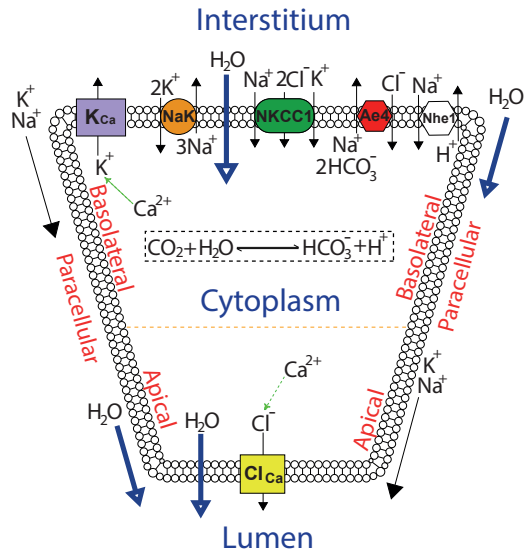


Fig. 2: Schematic diagram of the secretion model. Basolateral Nkcc1, NaK-ATPase, Ae4, Nhe1, and the Ca^{2+} -activated K^+ channels (K_{Ca}) are in charge of accumulating Cl^- in the cytoplasm. Opposite to these, the apical PM is equipped with Ca^{2+} -activated Cl^- channels (Cl_{Ca}) whose task is to extrude the accumulated Cl^- . Both apical and basolateral plasma membranes are permeable to water, which follows the osmotic gradient created by the transepithelial passage of Cl^- into the lumen. In this model there are paracellular K^+ and Na^+ currents along with a paracellular water flow (Sigüenza et al., 2018).

where j_{Nkcc1} and j_{Ae4} are the molar fluxes of Cl^- (with units of $\text{amol}/\mu\text{m}^2 \text{ sec}$) through the basolateral PM ($\partial\Omega_b$) and j_{Cl} the molar flux through the apical PM ($\partial\Omega_a$) Ca^{2+} -activated Cl^- channels. Performing the surface integrals and using the product rule we obtain:

$$\frac{d([\text{Cl}^-]_i)}{dt} = \frac{S_b}{\omega_i} 2J_{\text{Nkcc1}} + \frac{S_b}{\omega_i} J_{\text{Ae4}} - \frac{1}{\omega_i} \int_{\partial\Omega_a} j_{\text{Cl}} dS - \frac{d\omega_i}{dt} \frac{[\text{Cl}^-]_i}{\omega_i}, \quad (1)$$

where, S_b is the surface area of the basolateral PM. Note that the integral over the basolateral PM disappears, as these fluxes do not depend on Ca^{2+} . However, the integral over the apical membrane cannot be similarly reduced. This is because the apical Cl^- flux term depends on Ca^{2+} , which is spatially heterogeneous.

After performing the respective integrals, Eq. (1) describes how the intracellular Cl^- concentration changes over time (in units of mM/sec). The integral for the apical PM Cl^- flux term is described in more detail in section 3.3. The volume's (ω_i) rate of change with respect to time is given by the difference between basolateral and apical PM water fluxes (J^w) through aquaporins (PM water-selective channels):

$$\frac{d\omega_i}{dt} = J_a^w - J_b^w. \quad (2)$$

The luminal concentration equation is derived similarly. However, ω_l (the luminal volume) is kept constant, and using conservation laws the water flux out of the lumen is given by,

$$J_{\text{out}}^w = J_a^w + J_t^w \quad (3)$$

where J_t^w is the paracellular water flux through the tight junctions. Hence,

$$\frac{d([Cl^-]_l)}{dt} = \frac{1}{\omega_l} \int_{\partial\Omega_a} j_{Cl} dS - J_{out}^w \frac{[Cl^-]_l}{\omega_l}. \quad (4)$$

Following this approach, we obtain the following system of ordinary differential equations:

$$\omega_l \frac{d[Na^+]_l}{dt} = J_{Na}^t - J_{out}^w [Na^+]_l, \quad (5)$$

$$\omega_l \frac{d[K^+]_l}{dt} = J_K^t - J_{out}^w [K^+]_l, \quad (6)$$

$$\omega_l \frac{d[Cl^-]_l}{dt} = \int_{\partial\Omega_a} j_{Cl} dS - J_{out}^w [Cl^-]_l, \quad (7)$$

$$\frac{d\omega_i}{dt} = J_b^w - J_a^w, \quad (8)$$

$$\frac{d([Na^+]_i \omega_i)}{dt} = S_b \left(J_{Nkcc1} - 3J_{NaK} + J_{Nhe1} - J_{Ae4} \right), \quad (9)$$

$$\frac{d([K^+]_i \omega_i)}{dt} = S_b \left(J_{Nkcc1} + 2J_{NaK} \right) - \int_{\partial\Omega_b} j_K dS, \quad (10)$$

$$\frac{d([Cl^-]_i \omega_i)}{dt} = S_b \left(2J_{Nkcc1} + J_{Ae4} \right) - \int_{\partial\Omega_a} j_{Cl} dS, \quad (11)$$

$$\frac{d([HCO_3^-]_i \omega_i)}{dt} = \omega_i J_{Buffer} - S_b 2J_{Ae4}, \quad (12)$$

$$\frac{d([H^+]_i \omega_i)}{dt} = \omega_i J_{Buffer} - S_b J_{Nhe1}, \quad (13)$$

$$\left(\frac{C_m}{F}\right) \frac{dV_a}{dt} = \int_{\partial\Omega_a} j_{Cl} dS - (J_K^t + J_{Na}^t), \quad (14)$$

$$\left(\frac{C_m}{F}\right) \frac{dV_b}{dt} = - \int_{\partial\Omega_b} j_K dS - S_b J_{NaK} + (J_K^t + J_{Na}^t). \quad (15)$$

C_m and F are the PM capacitance and Faraday's constant, respectively. The conductances and densities of the system were chosen such that the resting states of the system are physiologically accurate. The various expresions of the transporters, exchangers, and ion channels used in this model are briefly presented in the Appendix. The parameters used here can be found in Table 1 in the Appendix. For further details on the specific details of the flux models refer to [Palk et al. \(2010\)](#), [Sigüenza et al. \(2018\)](#) and the companion paper [Pages et al. \(2018\)](#).

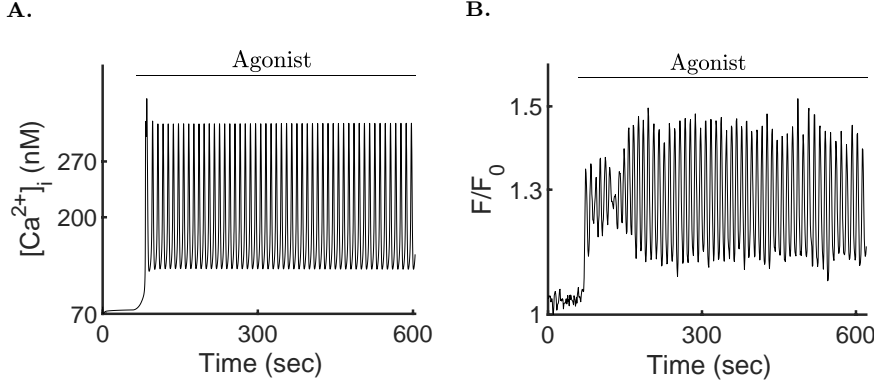


Fig. 3: **A.** Cell-wide average cytosolic $[Ca^{2+}]$ response to agonist. Our simulation is initiated such that $[Ca^{2+}]_i$ remains at its resting state (~ 72 nM) for a period of 60 sec before introducing agonist. Soon thereafter, the concentration oscillates around a plateau with a mean of ~ 200 nM. The result is presented and analysed in a companion paper (Pages et al., 2018). **B.** Experimental cytosolic $[Ca^{2+}]$, spatially averaged over the entire cell. Upon stimulation with the InsP₃-generating agonist ($[CCh]=300$ nM), oscillatory changes in the intracellular $[Ca^{2+}]$ of a parotid acinar cell can be observed (by means of the fluorescent Ca^{2+} indicator Fluo-4) for the duration of the agonist exposure.

3.3 Ca^{2+} Signalling

Full details of the Ca^{2+} signalling model are given in Pages et al. (2018). For convenience, some of the experimental data and a typical result from the Ca^{2+} dynamics model are reproduced in Fig. 3.

Water transport is driven by Ca^{2+} signalling with Ca^{2+} -dependent Cl^- channels in the apical membrane, and Ca^{2+} -dependent K^+ channels in the basal membrane. Here, the channel flux is described by:

$$J_c = \frac{G_c}{F} \left(V_{a,b} - \frac{RT}{Fz^c} \ln \left[\frac{[c]_{out}}{[c]_{inside}} \right] \right),$$

where $[c]$ represents the total concentration of either K^+ or Cl^- and the subscripts a apical, and b basolateral. The parameters R , T , F , and z^c denote the universal gas constant, temperature in Kelvin, Faraday's constant, and the valence of the ionic species (c), respectively. G_c is the channel conductance (dependent on $[Ca^{2+}]_i$) and is given by

$$G_c = \left(\frac{g_c}{S_{a,b}} \right) \int_{\partial\Omega_{a,b}} \left(\frac{[Ca^{2+}]_i^\eta}{K_c^\eta + [Ca^{2+}]_i^\eta} \right) dS, \quad (16)$$

where g_c is the whole cell maximum conductance, K_c represents the half-maximal activation concentration, η its Hill coefficient, $S_{a,b}$ the respective PM surface area, and $[Ca^{2+}]_i$ the local Ca^{2+} concentration.

To compute Eq. (16), we note that each node of the tetrahedral mesh comprising the PM surface ($\partial\Omega$) has a $[\text{Ca}^{2+}]_i$ value associated with it (Pages et al., 2018). The current (either K^+ or Cl^-) across each triangular surface face of the tetrahedral mesh is computed by calculating the average $[\text{Ca}^{2+}]$ on the surface triangle using the three values at the corners of the triangular face (i.e. the nodes of the mesh). This average $[\text{Ca}^{2+}]_i$ (\tilde{c}) is then used in Eq. (16) to calculate the K^+ or Cl^- current across that triangular face. Thus,

$$G_c = \left(\frac{g_c}{S_{a,b}} \right) \sum_{k=1}^N \int_{\partial\Omega_{a,b}^k} \left(\frac{\tilde{c}_k^\eta}{K_c^\eta + \tilde{c}_k^\eta} \right) dS_k. \quad (17)$$

Here, k denotes the k^{th} tetrahedral face comprising the respective PM surface ($\partial\Omega_{a,b}$), and N is the total number of tetrahedral faces in $\partial\Omega_{a,b}$. This procedure is repeated with every step of the numerical integration and incorporated into the equations for $[\text{Cl}^-]_l$, $[\text{Cl}^-]_i$, and $[\text{K}^+]_i$, accordingly.

4 Results

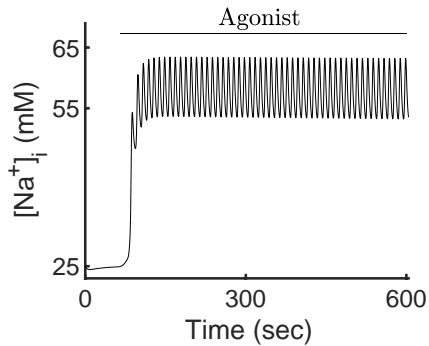
4.1 Ionic Concentrations, PM potentials, Cellular Volume, and Fluid Flow Rate

In order to mimic the experimental procedure shown in Fig. 3B, we initiated our simulation by setting the cytosolic $[\text{Ca}^{2+}]$ at rest (corresponding to the steady state value of ~ 72 nM) for a period of 60 sec before introducing agonist. Upon maximal stimulation (corresponding to 300 nM of the agonist CCh, $t > 60$ in Fig. 3), the cell-wide spatial average intracellular $[\text{Ca}^{2+}]$ reaches an oscillatory plateau with an average value of ~ 200 nM. The rest of the ionic concentrations, the PM potentials, and the cellular volume mirror the $[\text{Ca}^{2+}]_i$ and oscillate with the same frequency around a plateau for the duration of the agonist exposure (Figs. 4, 5, 6, and 7). For instance, the $[\text{Na}^+]_i$ oscillates with a relatively small amplitude around the mean value of 63.5 mM (Fig. 4A). This is consistent with the 2.5 fold increase, from rest, reported by Soltoff et al. (1989). The result reflects the complex interplay between the *NaK-ATPases*, the *Ae4* exchangers (which, together with the *NaK-ATPases*, extrude a large quantity of Na^+), and the electroneutral *Nhe1* antiporters whose task includes the re-introduction of extracellular Na^+ to promote an inwardly directed gradient whilst maintaining an adequate intracellular pH. The net Na^+ transport serves to energise the electroneutral cotransport of Cl^- by the basolateral *Nkcc1* cotransporters.

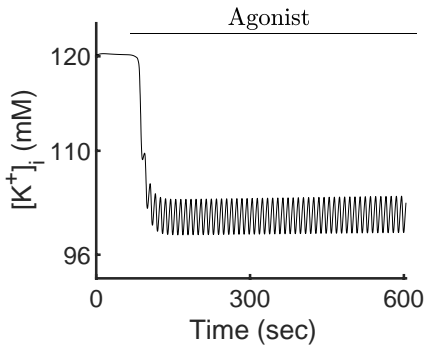
The $[\text{K}^+]_i$ can be seen decreasing by approximately 20% from its resting state of 120 mM to a mean value of ~ 97 mM (Fig. 4B). This result is in agreement with Poulsen and Bledsoe (1978) who reported an increase in interstitial $[\text{K}^+]$ increase of 2.2 to 18.7 meq/litre corresponding to the loss of intracellular K^+ after maximal cholinergic stimulation.

The cellular pH is consistent with Peña-Münzenmayer et al. (2015). The model indicates that the variation of $[\text{HCO}_3^-]_i$ is relatively small and the intracellular pH is approximately constant (Figs. 4C and 4D). This suggests that the complex dynamics between the *Ae4* and *Nhe1*, and their role as parallel Cl^- accumulation supporting mechanism, are within physiological agreement with what Sigüenza et al. (2018) reported.

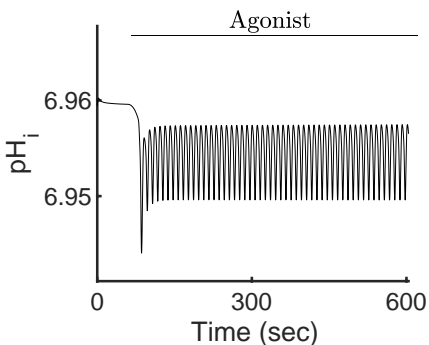
A.



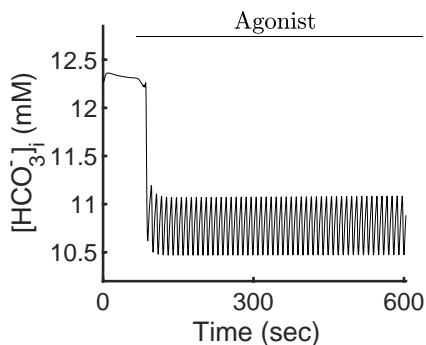
B.



C.



D.



E.

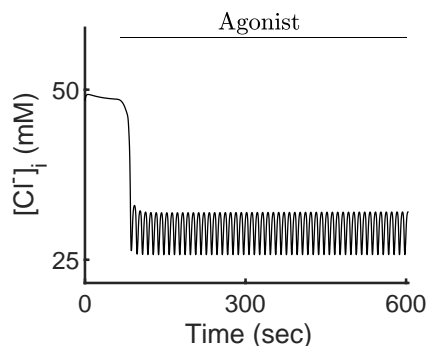
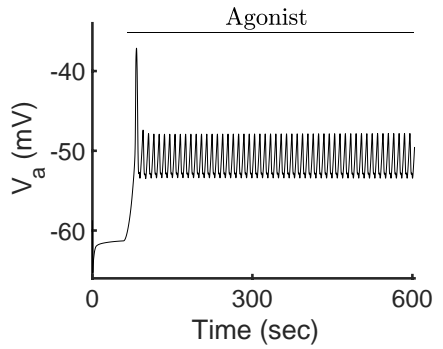


Fig. 4: Response of the intracellular ionic concentrations and intracellular pH to agonist-induced secretion. **A.** An increase in cytosolic $[Ca^{2+}]_i$ promotes an approximate 2.5 fold increase in the $[Na^+]_i$. The result is an improvement from previous models and is consistent with observations by Soltoff et al. (1989). **B.** A pronounced K^+ efflux serves to hyperpolarise the membrane and sustain apical Cl^- efflux. Our model reproduces the behaviour reported by Poulsen and Bledsoe (1978). **C & D.** The pH and $[HCO_3^-]_i$ are seen varying relatively little, in agreement with Peña-Münzenmayer et al. (2015). **E.** Upon secretion, the $[Cl^-]_i$ decreases to $\sim 50\%$ of its resting value during each oscillation. The result is the hallmark of water secreting epithelia (Silva et al., 1977).

A.



B.

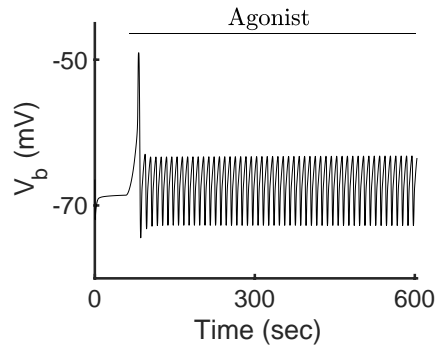
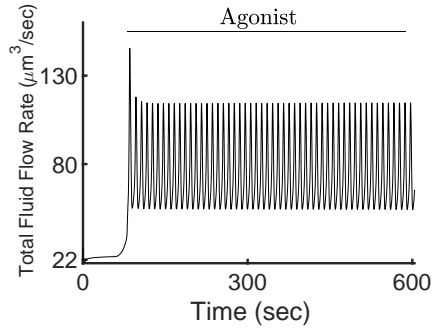


Fig. 5: Response of cellular PM potentials, to changes in $[Ca^{2+}]_i$ upon agonist stimulation. **A** shows the apical potential & **B** shows the basal potential. As $[Ca^{2+}]_i$ in the apical region reaches its maximum value, the negatively outward directed current depolarises the entire plasma membrane, but soon thereafter (nearly instantaneously) the basolateral $[Ca^{2+}]_i$ activates a K^+ current that hyperpolarises the PM and sustains the apical Cl^- efflux.

A.



B.

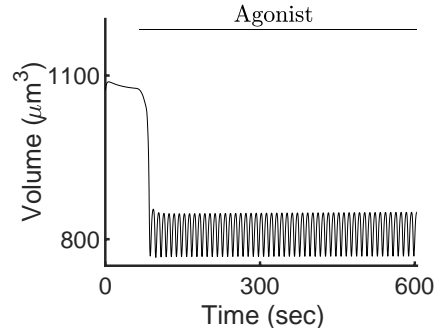


Fig. 6: Response of the cellular volume and fluid flow rate to changes in the cytosolic $[Ca^{2+}]_i$ upon agonist stimulation. **A.** During secretion, the fluid flow rate reaches an oscillating plateau with a mean value of $\sim 78 \mu\text{m}^3/\text{sec}$ above its resting value of $22 \mu\text{m}^3/\text{sec}$. **B.** Experimental observations in parotid epithelia demonstrate that the transcellular passage of water is responsible for an approximate 30% decrease in cellular volume (Melvin et al., 2005). Our model exhibits a volume decrease of approximately 27% of its resting value for the duration of the agonist exposure.

Upon agonist stimulation, apically localised inositol 1,4,5-trisphosphate ($InsP_3$) receptors release Ca^{2+} from internal stores causing the activation of neighbouring apical Cl^- channels resulting in a drop in $[Cl^-]_i$ to approximately 50% of its resting value (Fig. 4E). This causes a fast apical PM depolarisation (Fig. 5). Note that if this depolarisation were to continue, it would prevent the efflux of Cl^- and consequently stop water transport. To prevent this, a slightly delayed increase in basolateral $[Ca^{2+}]_i$ causes rapid activation of the basolateral $IK/BK1$ channels allowing

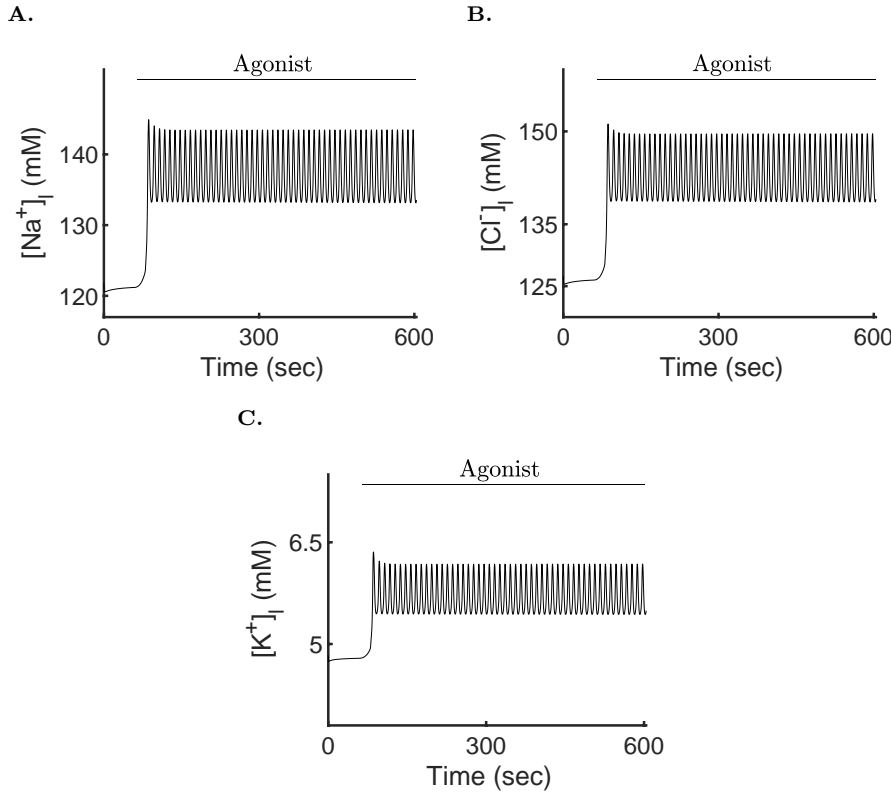


Fig. 7: Luminal ionic response to changes in cytosolic $[Ca^{2+}]_i$. **A & B.** At maximal stimulation, the $[Na^+]_l$ and $[K^+]_l$ reach an oscillating plateau $\sim 15\%$ larger than their respective resting values. Note how the luminal concentration of Cl^- is higher than that of Na^+ . This is because the paracellular movement of Na^+ and K^+ ions through the tight junction into the lumen requires a lumen negative driving force. **C.** The $[K^+]_l$ in the lumen is relatively low, in agreement with [Mangos et al. \(1973\)](#).

K^+ to exit towards the interstitial compartment. The cation efflux decreases the basolateral and apical PM potentials, thus maintaining apical Cl^- efflux.

It is interesting to note that the responses of the apical and basolateral membrane potentials are not simple oscillations, but have a complicated structure. This is because any change in voltage at either membrane portion is mirrored in the other membrane section. For example, when apical Ca^{2+} increases this causes an immediate increase in the apical Cl^- current, and thus an immediate depolarisation of both the apical and basolateral plasma membranes. The subsequent increase in basal Ca^{2+} then increases the basal K^+ current, which hyperpolarises the basolateral PM, but also reduces the potential of the apical PM. Thus, both V_a and V_b show complex responses with multiple peaks and troughs.

The salivary flow rate changes from a resting state of 22 to a $\sim 78 \mu\text{m}^3/\text{sec}$ mean upon agonist-induced $[Ca^{2+}]_i$ increases (Fig. 6A). Fluid flow rate experiments in mouse parotid glands, demonstrated that cholinergic-induced secretion results

in a gland secretory rate of approximately 11 to 16 $\mu\text{L}/\text{min}$ (Evans et al., 2000; Romanenko et al., 2010). Accordingly, our model estimates about 2.86×10^6 cells in a typical mouse parotid gland. This is an improvement from previous mathematical models in which the flow did not attain a physiological rate (Gin et al., 2007; Palk et al., 2010; Sigüenza et al., 2018). Water transport causes a decrease in cellular volume of approximately 29% (Fig. 6B), in agreement with Foskett et al. (1991). The electrolyte concentration of primary saliva produced by the model has a relatively high concentration of Na^+Cl^- , whilst $[\text{K}^+]_i$ is relatively low (Fig. 7), consistent with Mangos et al. (1973).

5 Effects of Calcium Signalling in Fluid Secretion

The following results correspond to a series of ‘in-silico’ experiments with distinct variations of the model presented in Section 4. We define:

- **Model 1** to be the model whose results are presented in Figs. 4–7. It corresponds to the secretion model solved in conjunction with the spatially heterogeneous, and oscillating in time, Ca^{2+} signalling model (described in Pages et al., 2018).
- **Model 2** is the secretion model driven by the mean apical and the mean basal $[\text{Ca}^{2+}]$. Note that each of these spatial means will be oscillating in time.
- **Model 3** is the secretion model driven by the mean apical and the mean basal $[\text{Ca}^{2+}]$, where (as opposed to **Model 2**) the means are now taken in both space and time. Thus, water secretion in **Model 3** is driven by a constant apical and a constant basal $[\text{Ca}^{2+}]$.
- **QSS Model** is a quasi-steady state (QSS) approximation of the fluid secretion model. Here, water secretion is assumed to be an algebraic function of the mean $[\text{Ca}^{2+}]$, where the mean is now taken over the entire cell at each point in time. Thus, in this model, the mean $[\text{Ca}^{2+}]$ is oscillating, but is the same in both the apical and basal regions.

Apical and basolateral heterogeneities

We analysed the distribution of Cl^- and K^+ current densities given by *Model 1*. Figs. 8A and 8B depict a spread of surface current density values across the tetrahedral faces that form the apical and basolateral plasma membranes of the cell, respectively. These correspond to the different values of peak $[\text{Ca}^{2+}]_i$ during a period of the oscillation. Fig. 8A shows that the majority of the apical Cl^- current ($\sim 76\%$) peaks at approximately $140 \text{ pA}/\mu\text{m}^2$. Similarly, Fig. 8B shows that the majority of the basal K^+ current peaks at $220 \text{ pA}/\mu\text{m}^2$. Given the large number of triangular faces in the PM with approximately similar surface current density, we hypothesised that only the spatial $[\text{Ca}^{2+}]_i$ mean at the apical and basolateral regions of the cell may be needed to attain an appropriate secretion rate. To test this, we computed the fluid flow rate using the cytosolic $[\text{Ca}^{2+}]$ spatial mean response to agonist stimulation at the apical and basolateral regions of the cell (Fig. 8C). The

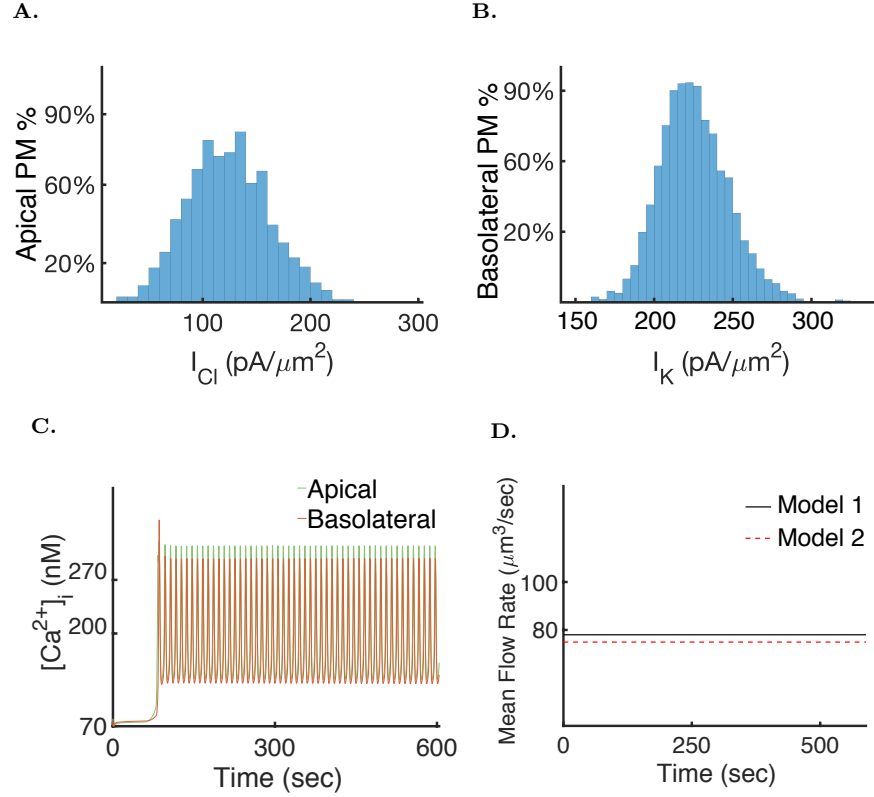


Fig. 8: **A.** Distribution of the Cl^- surface current densities of *Model 1* at maximal $[Ca^{2+}]_i$, as a function of the percentage of tetrahedral faces that form the apical PM. The majority reach a maximal Cl^- current of approximately $140 \text{ pA}/\mu\text{m}^2$. **B.** Distribution of K^+ surface current densities of *Model 1* as a function of the percentage of triangular faces that form the basolateral PM at maximum $[Ca^{2+}]_i$. The majority reach a maximal K^+ current of approximately $220 \text{ pA}/\mu\text{m}^2$. **C.** *Model 2*. Spatial mean of the $[Ca^{2+}]_i$ response to agonist stimulation at the apical (green) and basolateral (orange) cellular regions. **D.** Mean fluid flow rate of *Model 2* (red) compared to the mean fluid flow rate of *Model 1* (black). *Model 2* gives an 8% decrease in mean flow rate compared to *Model 1*. The result indicates that the signalling heterogeneities in the apical and basal regions, exhibited in *Model 1*, are not necessary to drive a physiological secretion rate.

results, shown in Fig. 8D (denoted as *Model 2*), indicate that the spatial heterogeneities of the $[Ca^{2+}]_i$ exhibited in *Model 1* have little impact on the mean saliva secretion rate.

Effects of oscillations on fluid flow.

Palk et al. (2012) reported that using the spatio-temporal mean of an oscillating $[Ca^{2+}]_i$ to drive water transport, in an earlier secretion model, resulted in an almost identical flow rate as when using its oscillating counterpart. Thus, they concluded, this was sufficient to drive secretion when the flow rate is the only modelling con-

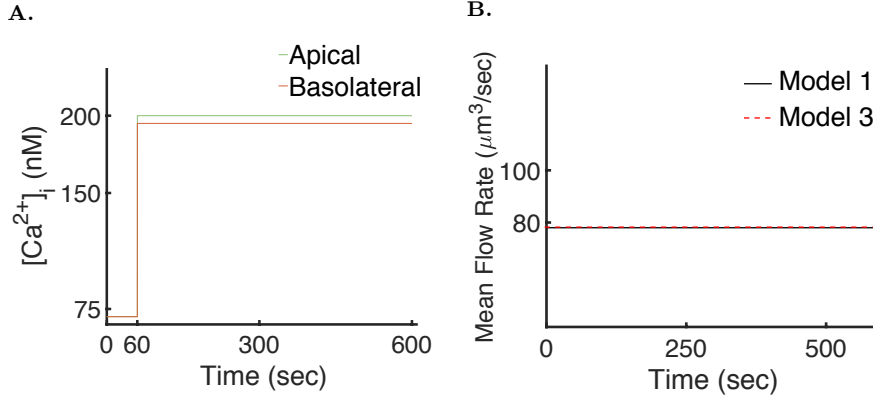


Fig. 9: **A.** *Model 3*. Spatio-temporal mean of the apical and the basolateral cytosolic [Ca²⁺] responses to agonist stimulation. Here both [Ca²⁺]_i, the apical (green) and the basolateral (orange), elevate from rest into a sustained non-oscillatory plateau upon agonist stimulation. **B.** Mean flow rate of *Model 3* compared to the mean flow rate given by *Model 1*. The mean rate generated by *Model 3* is identical to the mean rate given by *Model 1*. The figure shows that only the [Ca²⁺]_i spatio-temporal mean is needed to drive secretion to physiological levels. Our result supports a previous hypothesis by Palk et al. (2012).

cern (as in Sigüenza et al. (2018)). We thus simulated *Model 3* the spatio-temporal mean of the apical and basolateral cytosolic [Ca²⁺] response to agonist stimulation (see Fig. 9A). Results reveal that using the spatio-temporal mean [Ca²⁺]_i to drive secretion generates a mean flow rate almost identical to the one given by *Model 1* (Fig. 9B). Our result validates the findings of Palk et al. (2012), and indicates that the spatio-temporal patterns emerging from Ca²⁺ signalling are not an important determining factor when it comes to secretion. Interestingly, if saliva secretion is driven by a Ca²⁺ model that exhibits low-frequency baseline spiking, the oscillation period and shape has a large effect on saliva secretion (results not shown). Thus, we conclude that the insensitivity of saliva secretion to the frequency and shape of the oscillations is a result of the fact that the oscillations are of high frequency and on a raised baseline. In saliva secreting cells, [Ca²⁺]_i oscillations are invariably of this type.

Quasi-steady-state approximation

We next consider how the time scales involved in the various ionic currents and changes in cell volume affect saliva secretion. For a given fixed [Ca] (across the entire cell) the fluid flow can be calculated. When this is done for a range of fixed [Ca] we can then derive a relationship between steady-state [Ca²⁺]_i and fluid flow. This relationship is plotted in Figure 10A. The functional relationship is given by,

$$f_{\text{FR}}([{\text{Ca}}^{2+}]_i) = V \left(\frac{[{\text{Ca}}^{2+}]_i^{3.5}}{K + [{\text{Ca}}^{2+}]_i^{3.5}} \right),$$

where, $V = 91$ and $K = 3 \times 10^{-4}$.

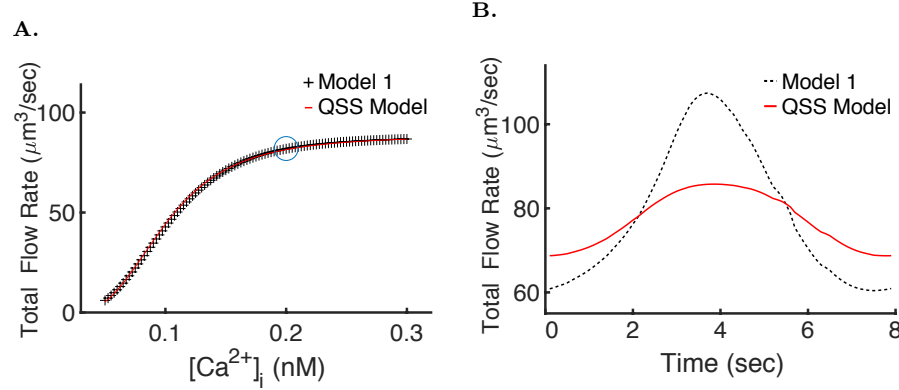


Fig. 10: **A.** *QSS Model*. We fitted a Hill-function (red) to the flow rate steady-states of the secretion model. These were driven by the cell-wide spatio-temporal mean $[Ca^{2+}]_i$ responses to different agonist concentrations (dotted black curve). **B.** Single flow rate oscillation given by the *QSS Model* (red) driven by the cell-wide spatial $[Ca^{2+}]_i$ mean, against the flow rate given by *Model 1* (black). The *QSS Model* gives a reasonably accurate prediction of the mean flow rate.

In Fig. 10B we present a comparison between the *QSS Model* (driven by the cell-wide spatial, but not temporal, mean $[Ca^{2+}]$ see Fig. 3A) and *Model 1* flow rates (Fig. 6A). Although the shape of the flow rate curves differ, the mean fluid secretion rate is almost identical. The result indicates that a quasi-steady-state approximation to the saliva secretion model gives a reasonably accurate prediction of the flow rate and if modelling the latter is the only goal, the *QSS Model* suffices. However, in doing so, all the dynamic complexity, not only of the fluid secretion mechanism but also of the intracellular heterogeneity of cytosolic $[Ca^{2+}]$, is ignored.

This is a startling result, potentially of great importance for future attempts at model simplification. It shows that, although in our current model some of the time scales of the ionic currents (or those of volume change) affect total fluid flow, the entire model can be replaced by a QSS curve that algebraically relates spatially averaged $[Ca^{2+}]_i$ to fluid flow. Thus, in a more complex multicellular setting, the entire fluid flow model (in each cell) could potentially be replaced by an algebraic relationship that could be computed separately (for each cell), leading to an enormous increase in simulation speed.

As yet we have performed no detailed analysis of this result (for example, to what extent does the volume affect the result?) and so it is not yet possible to say with certainty that the fluid flow model for any realistic parotid cell can always be reduced to a single algebraic relationship between saliva secretion and $[Ca^{2+}]_i$. Nevertheless, the possibilities are intriguing.

5.1 Other Cells

Until now we have concentrated on discussing the results from a single cell. To demonstrate that our model works in any given cell, we solved *Model 1* in seven different cells, each of which has a different shape and volume constructed from a

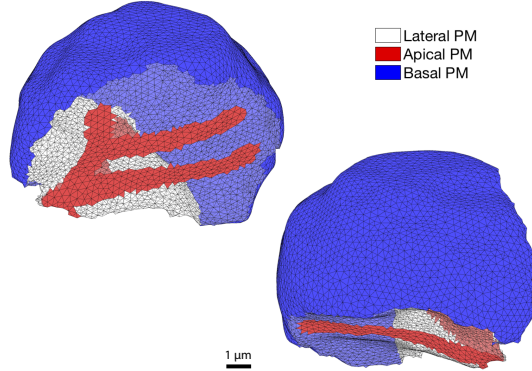


Fig. 11: Tetrahedral mesh depicting a salivary gland acinar cell constructed by Pages et al. (2018). Two images of the same cell are shown, where the cell is rotated to exhibit the apical (red) and basal (blue) regions of the cellular plasma membrane. The non-coloured triangular faces represent the lateral portion.

z stack of confocal slices. The results can be found in the supplementary material. Here, we briefly present the results from one of the other cells. Fig. 11 shows the cellular mesh created by Pages et al. (2018). From Figs. 12 and 13 we see that the model reproduces critical experimental data for this cell also, including the expected changes in cellular volume and the concentrations of the ionic species involved in fluid secretion.

6 Discussion

Ca^{2+} signalling plays a pivotal role in the process of water transport regulation by salivary epithelia. The second messenger modulates the activation of PM channels, providing the cell with a means of control for the efflux and influx of Cl^- and ultimately fluid secretion. Although secretion models that include Ca^{2+} signalling exist, up until now the majority have been based on highly simplified dynamics (Gin et al., 2007; Palk et al., 2010, 2012; Sigüenza et al., 2018). In this study we used a physiologically accurate Ca^{2+} signalling model, solved on seven anatomically-accurate domains, to drive fluid secretion. The Ca^{2+} model is described in detail in a companion paper (Pages et al. 2018). Our aim was to investigate how the structure of the cells and the heterogeneity of the Ca^{2+} dynamics affects saliva secretion.

We found that our model successfully reproduces the observed physiological responses of salivary epithelia upon agonist-induced stimulation, including the expected changes in cell volume and the relevant ionic concentrations involved in the transport of water (Figs. 4 and 7). The addition of the spatio-temporal Ca^{2+} -signalling model to drive fluid secretion resolves several problems encountered in previous models. For instance, the $[\text{Na}^+]_i$ increases approximately 2.5 fold upon agonist-stimulation, a result seen often in experimental settings (Figs. 4A). The result is an improvement from earlier models which display only an increase of 30% above the rest state (Palk et al., 2010; Sigüenza et al., 2018). Similarly, Foskett (1990) observed a decrease of approximately 50% in cytosolic $[\text{Cl}^-]_i$ upon stimulation, and our model successfully reproduces their results. As a consequence, the cell volume decreases by approximately 29% (Naumtofte, 1992). The mean fluid flow rate of the model upon agonist-induced stimulation is $\sim 78 \mu\text{m}^3/\text{sec}$ or a ~ 4 fold increase

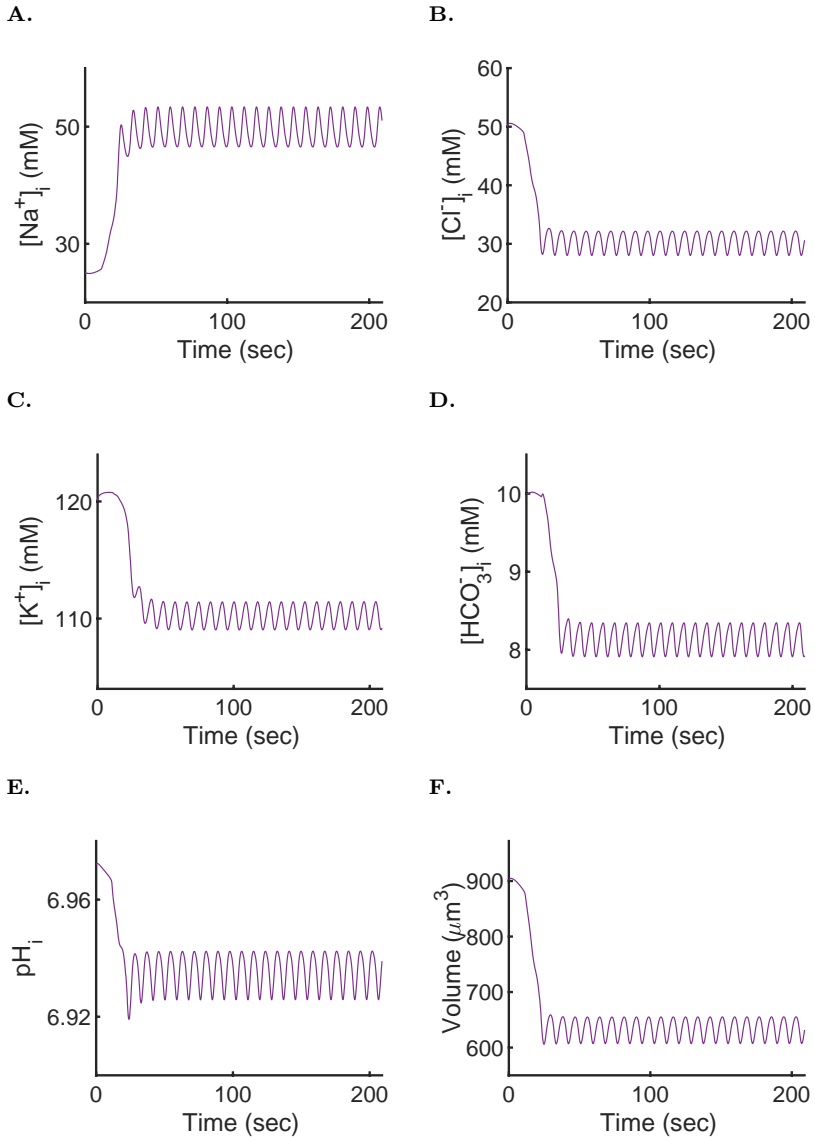


Fig. 12: Intracellular concentrations, pH, and volume responses to agonist stimulation in the cell shown in Fig. 11

from rest (Fig. 6A). Although the figure seems low, given that [Sigüenza et al. \(2018\)](#) claim a 12 fold increase, this is because we based our model on experiments which use only 300 nM of CCh agonist to induce Ca^{2+} responses. In [Peña-Münzenmayer et al. \(2015\)](#), the study that [Sigüenza et al. \(2018\)](#) results are based on, they use 2 agonists, CCh and isoproterenol (IPR), to stimulate secretion. This results in a larger $[\text{Ca}^{2+}]_i$, ultimately elevating the secretion rate to a 12 fold increase above rest. Nevertheless, our result is an improvement on previous models in which the

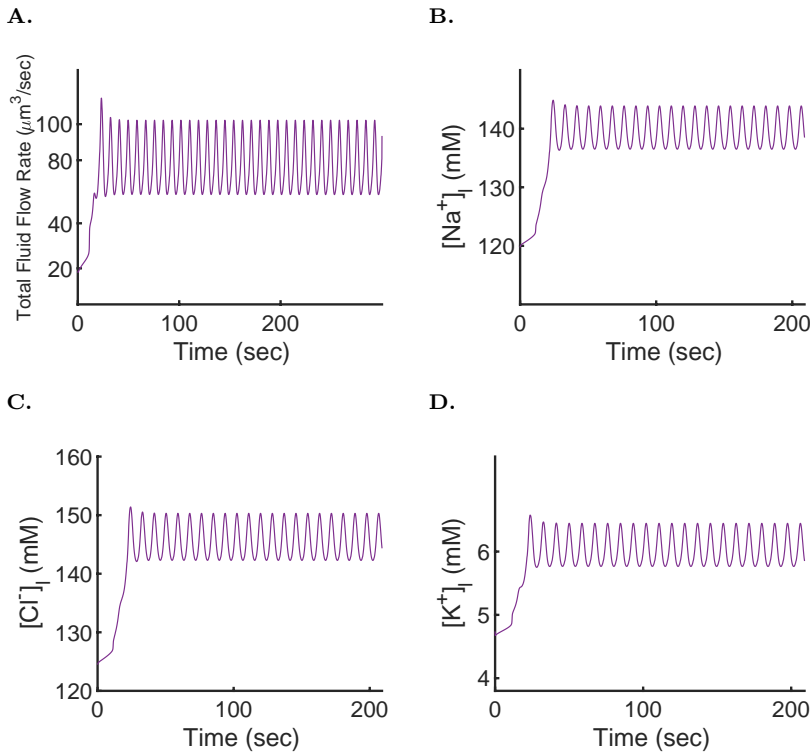


Fig. 13: Fluid flow and luminal concentrations upon agonist stimulation in the cell shown in Fig. 11.

fluid flow rate increases by only 2 to 2.5 fold from rest under similar conditions to our model (Gin et al., 2007; Palk et al., 2010). Furthermore, Evans et al. (2000) observed a volume of 400 μL per 100 mg of parotid gland in 50 min. We estimated that an upper bound of approximately 2.86×10^6 acinar cells exist in 100 mg of parotid gland. According to this figure, our model's results are consistent with experimental data.

Here, as in previous studies, the secretion model includes two coupled PM potentials to account for the polarised nature of acinar cells (Palk et al., 2010; Sigüenza et al., 2018). However, the corresponding responses (apical and basolateral) to the transmembrane movement of ions display complicated oscillatory structures previously unreported in primary saliva models (Figs. 5A and 5B). Our results show that following a $[\text{Ca}^{2+}]_i$ increase in the apical region, an immediate depolarisation of both plasma membranes occurs. Shortly thereafter, as a consequence of the relay of Ca^{2+} signals towards the basolateral region, a delayed hyperpolarisation of the basolateral PM occurs, causing a reduction of the apical PM potential. The coupling of both membranes is evident here, as a change in voltage at either membrane portion is mirrored by the other.

Measuring the response of apical Cl^- and basolateral K^+ currents revealed that the majority of the PM surface reaches a similar Cl^- and K^+ current density (Figs. 8A and 8B). Interestingly, these correspond to the current densities given by the average apical and basolateral $[\text{Ca}^{2+}]_i$ traces (Fig. 8C). The observation suggests that averaging the $[\text{Ca}^{2+}]_i$ at each region (basolateral and apical) would yield the same fluid flow as would a heterogeneous distribution of $[\text{Ca}^{2+}]_i$ in the cell. When this hypothesis is tested (Fig. 8D) we see that the fluid flow rate obtained by averaging the $[\text{Ca}^{2+}]_i$ in each region produces the same result as its heterogeneous counterpart. We propose that heterogeneity of $[\text{Ca}^{2+}]_i$ in the apical and basal regions is not an important mechanism in the secretion process. Thus, at least for modelling purposes, we claim that to predict and understand the acinar secretion, a three dimensional model of Ca^{2+} signalling is, perhaps, not necessary. Instead, a simpler ordinary differential equation model describing the signalling phenomena that reproduces the appropriate Ca^{2+} responses at each end of the cell may be sufficient.

Perhaps one of the most important results, and a prediction of our study, stemmed from computing the fluid flow rate of the system using a spatio-temporal homogeneous distribution of apical and basolateral $[\text{Ca}^{2+}]_i$ - denoted *Model 3* in Section 5 (see Fig. 9A). The resultant non-oscillating mean flow rate was found to be nearly identical to its oscillating counterpart - given by *Model 1* (see Fig. 9B). Palk et al. (2012) suggested that driving secretion using the spatio-temporal mean of a $[\text{Ca}^{2+}]_i$ oscillation, results in an accurate flow rate. Our result supports their hypothesis. Although Palk et al. (2012) never tested this with an accurate Ca^{2+} model, it is evident now that because of the high frequency $[\text{Ca}^{2+}]_i$ oscillations, the only important factor determining secretion is the temporal mean $[\text{Ca}^{2+}]_i$.

Our secretion model can possibly be simplified even further, as long as the only output of interest is the mean fluid flow. Eq. (5) assumes a quasi-steady state approximation to the rate of change in cellular volume and the associated ionic concentrations in order to compute the fluid flow rate as a function of $[\text{Ca}^{2+}]_i$. Using the cell-wide cytosolic $[\text{Ca}^{2+}]$ spatial mean, we compared the solution of *Model 1* to the solution using this quasi-steady state approximation (Fig. 9B), and found that mean saliva secretion was identical. Although we have not tested this result exhaustively, it raises the intriguing possibility that an accurate model of fluid flow may be constructed by assuming that all ionic flows and cell volume changes are at quasi-steady state, and thus that their dynamic responses have little effect on fluid secretion. One possible difficulty with this simplified approach is that our present model does not include an accurate model of bicarbonate buffering. It is possible that slower time scales involved in pH control and bicarbonate buffering will make a quasi-steady state assumption inaccurate, but resolution of this question awaits further work.

Lastly, our simulations were performed using the Sigüenza et al. (2018) model for fluid secretion. However, we simplified their model by omitting the basolateral $\text{Cl}^-/\text{HCO}_3^-$ Anion Exchanger 2, and assuming that $[\text{CO}_2]$ is constant. It has been shown mathematically, and experimentally, that the $Ae2$ is not important for fluid secretion. Furthermore, Sigüenza et al. (2018) show that throughout stimulation and the rest phases of secretion $[\text{CO}_2]$ is constant, as is pH. Thus, in our pursuit of

computational simplicity we set $[CO_2]$ to be constant. It is unclear how much of a difference this simplifying assumption makes. However, it remains possible that, for some cells and for some parameters, the dynamics of pH and bicarbonate buffering will introduce time scales that have a more significant impact on the rate of saliva secretion. This is a question that will be explored in further work.

In summary, the exact details of the cytosolic $[Ca^{2+}]$ heterogeneity seem to matter little. Our study still does not resolve to what extent does the propagation of Ca^{2+} waves, from apical to basolateral affect the secretory process due to the high frequency of $[Ca^{2+}]_i$ oscillations. What we can infer from our results, however, is that these waves occur very fast, resulting in a near instantaneous Ca^{2+} response across the cell as reported by [Giovannucci et al. \(2002\)](#). But based on the results of our study, we claim that a partial differential equation model of Ca^{2+} signalling may not be necessary to attain a physiological secretion rate in this model. When combined with the fact that the dynamics of ion currents and cell volume control appear to be unimportant if the only modelling concern is flow rate, we conclude that an accurate model of saliva secretion could possibly be constructed by a small system of ODEs coupled with an algebraic function describing secretion as a function of $[Ca^{2+}]_i$. Such an extreme simplification, if shown to be reliably accurate, would make multicellular and multiscale computations possible and efficient.

Acknowledgements

This work was supported by the U.S. National Institutes of Health (NIDCR) grant RO1DE019245-10 (ES, DY, and JS) and the Marsden Fund of the Royal Society of New Zealand grant 3708441 (NP and JS). High-performance computing facilities and support were provided by the New Zealand eScience Infrastructure (NeSI). Funded jointly by NeSI's collaborator institutions and through the Ministry of Business, Innovation and Employment's Research Infrastructure programme (ES, NP, JS, and JR). Finally, we would like to thank NVIDIA Corporation for a K40 GPU grant (JR).

Appendix

1 . Fluxes of the Model

$$j_{\text{NaK}} = \alpha_{\text{NaK}} \left(r \frac{[\text{K}^+]_e^2 [\text{Na}^+]_i^3}{[\text{K}^+]_e^2 + \alpha [\text{Na}^+]_i^3} \right), \quad (18)$$

(19)

$$j_{\text{Nkcc1}} = \alpha_{\text{Nkcc1}} \left(\frac{a_1 - a_2 [\text{Na}^+]_i [\text{K}^+]_i [\text{Cl}^-]_i^2}{a_3 + a_4 [\text{Na}^+]_i [\text{K}^+]_i [\text{Cl}^-]_i^2} \right), \quad (20)$$

$$j_{\text{Nhe1}} = G_{\text{Nhe1}} \left(\frac{[\text{H}^+]_i}{[\text{H}^+]_i + K_{\text{H}}} \right)^2 \left(\frac{[\text{Na}^+]_e}{[\text{Na}^+]_e + K_{\text{Na}}} \right), \quad (21)$$

$$J_{\text{Ae4}} = G_{\text{Ae4}} \left(\frac{[\text{Cl}^-]_e}{[\text{Cl}^-]_e + K_{\text{Cl}}} \right) \left(\frac{[\text{Na}^+]_i}{[\text{Na}^+]_i + K_{\text{Na}}} \right) \left(\frac{[\text{HCO}_3^-]_i}{[\text{HCO}_3^-]_i + K_{\text{B}}} \right)^2, \quad (22)$$

$$J_{\text{Buffer}} = k_1 [\text{CO}_2]_i - k_{-1} [\text{H}^+]_i [\text{HCO}_3^-]_i \quad (23)$$

$$J_{\text{Na}^+}^t = \frac{G_{\text{Na}^+}^t}{Fz^{Na}} \left[V_a - V_b - \frac{RT}{F} \ln \left(\frac{[\text{Na}^+]_l}{[\text{Na}^+]_e} \right) \right], \quad (24)$$

$$J_{\text{K}^+}^t = \frac{G_{\text{K}^+}^t}{Fz^K} \left[V_a - V_b - \frac{RT}{F} \ln \left(\frac{[\text{K}^+]_l}{[\text{K}^+]_e} \right) \right].$$

2 . Water Fluxes

$$J_a^w = P_a \left(\sum [c]_l + \Psi_l - \sum [c]_i - \frac{x_i}{\omega_i} \right), \quad (25)$$

(26)

$$J_b^w = P_b \left(\sum [c]_i + \frac{x_i}{\omega_i} - \sum [c]_e \right), \quad (27)$$

$$J_t^w = P_t \left(\sum [c]_l + \Psi_l - \sum [c]_e \right).$$

Where,

$$\sum [c]_e = [\text{K}^+]_e + [\text{Na}^+]_e + [\text{Cl}^-]_e + [\text{HCO}_3^-]_e + [\text{H}^+]_e + [\text{CO}_2]_e,$$

$$\sum [c]_i = [\text{K}^+]_i + [\text{Na}^+]_i + [\text{Cl}^-]_i + [\text{HCO}_3^-]_i + [\text{H}^+]_i + [\text{CO}_2]_i,$$

$$\sum [c]_l = [\text{K}^+]_l + [\text{Na}^+]_l + [\text{Cl}^-]_l + [\text{HCO}_3^-]_l + [\text{H}^+]_l.$$

The parameter x_i denotes the amount of negatively charged ions with valence $z = -1$ **impermeable** to the cellular PM. Its value is determined by imposing electroneutrality in the cellular compartment. Note that all compartments of the model are assumed electroneutral at all times. The parameter Ψ_l in Eq.(26) represents the concentration of uncharged impermeable species present in the lumen, including (but not limited to) proteins such as amylase and big molecules like CO_2 .

3 . Parameters of the Model

Table 1: Table of Parameters

Parameter	Description	Value	Units
w_0	Cellular Volume	1105.44	μm^3
S_a	Apical Surface Area	95.25	μm^2
S_b	Basal Surface Area	284.75	μm^2
α_{NaK}	Membrane surface density	1.6	$\text{amol}/\mu\text{m}^2$
α_{Nkcc1}	Membrane surface density	2.15	$\text{amol}/\mu\text{m}^2$
G_{Nhe1}	Membrane surface density	0.9	$\text{amol}/\mu\text{m}^2$
G_{Ae4}	Membrane surface density	1.3	$\text{amol}/\mu\text{m}^2$
G_{Na}^t	Conductance	0.2	nS
G_{K}^t	Conductance	0.16	nS
r	NaK-ATPase rate	0.0016	$\text{mM}^{-3} \text{ s}^{-1}$
a_1	Nkcc1 rate	157.55	s^{-2}
a_2	Nkcc1 rate	2.009×10^{-5}	$\text{mM}^{-4} \text{ s}^{-2}$
a_3	Nkcc1 rate	1.0306	s^{-1}
a_4	Nkcc1 rate	1.38×10^{-6}	$\text{mM}^{-4} \text{ s}^{-1}$
K_H	Half half maximal H^+ concentration	4.5×10^{-4}	mM
K_{Na}	Half half maximal Na^+ concentration	15	mM
K_{Cl}	Half half maximal Na^+ concentration	5.6	mM
K_B	Half half maximal Na^+ concentration	1e4	mM
k_n	HCO_3^- Buffer Dissociation rate	0.132	s^{-1}
k_p	HCO_3^- Buffer Association rate	312	s^{-1}
z_{Na}^+	Na^+ valence	+1	-
z^K	K^+ valence	+1	-
P_a	Apical PM water permeability	4.43	$\mu\text{m}^3 \text{ mM}^{-1} \text{ s}^{-1}$
P_b	Basolateral PM water permeability	1.94	$\mu\text{m}^3 \text{ mM}^{-1} \text{ s}^{-1}$
P_t	Tight junction's water permeability	0.05	$\mu\text{m}^3 \text{ mM}^{-1} \text{ s}^{-1}$
Ψ_l	Luminal uncharged particles	51.74	mM

References

- Almassy J., Won J. H., Begenisich T. B., Yule D. I. (2012) Apical Ca^{2+} -activated potassium channels in mouse parotid acinar cells. *J Gen Physiol* 139(2):121–133, <https://doi.org/10.1085/jgp.201110718>
- Almássy J., Siguenza E., Skalickzi M., Matesz K., Sneyd J., Yule D. I., Nánási P. P. (2018) New saliva secretion model based on the expression of Na^+ - K^+ pump and K^+ channels in the apical membrane of parotid acinar cells. *Pflugers Arch* 470(4):613–621, <https://doi.org/10.1007/s00424-018-2109-0>
- Evans R. L., Park K., Turner R. J., Watson G. E., Nguyen H.-V., Dennett M. R., Hand A. R., Flagella M., Shull G. E., Melvin J. E. (2000) Severe impairment of salivation in $\text{Na}^+/\text{K}^+/2\text{Cl}^-$ cotransporter (NKCC1)-deficient mice. *J Biol Chem* 275(35):26,720–26,726, <https://doi.org/10.1074/jbc.M003753200>
- Foskett J. (1990) $[\text{Ca}^{2+}]_i$ modulation of Cl^- content controls cell volume in single salivary acinar cells during fluid secretion. *Am J Physiol Cell Physiol* 259(6 Pt 1):C998–C1004, <https://doi.org/10.1152/ajpcell.1990.259.6.C998>
- Foskett J., Roifman C., Wong D. (1991) Activation of calcium oscillations by thapsigargin in parotid acinar cells. *J Biol Chem* 266(5):2778–2782
- Foskett J. K., Melvin J. E. (1989) Activation of salivary secretion: coupling of cell volume and $[\text{Ca}^{2+}]_i$ in single cells. *Science* 244(4912):1582–1585
- Gin E., Crampin E. J., Brown D. A., Shuttleworth T. J., Yule D. I., Sneyd J. (2007) A mathematical model of fluid secretion from a parotid acinar cell. *J Theor Biol* 248(1):64–80, <https://doi.org/10.1016/j.jtbi.2007.04.021>
- Giovannucci D. R., Bruce J. I., Straub S. V., Arreola J., Sneyd J., Shuttleworth T. J., Yule D. I. (2002) Cytosolic Ca^{2+} and Ca^{2+} -activated Cl^- current dynamics: insights from two functionally distinct mouse exocrine cells. *J Physiol* 540(2):469–484
- Mangos J., McSherry N. R., Nousia-Arvanitakis S., Irwin K. (1973) Secretion and transductal fluxes of ions in exocrine glands of the mouse. *Am J Physiol* 225(1):18–24, <https://doi.org/10.1152/ajplegacy.1973.225.1.18>
- Martin C., Young J. (1971) Electrolyte concentrations in primary and final saliva of the rat sublingual gland studied by micropuncture and catheterization techniques. *Pflugers Archiv* 324(4):344–360
- Melvin J. E., Yule D., Shuttleworth T., Begenisich T. (2005) Regulation of fluid and electrolyte secretion in salivary gland acinar cells. *Annu Rev Physiol* 67:445–469, <https://doi.org/10.1146/annurev.physiol.67.041703.084745>
- Nauntofte B. (1992) Regulation of electrolyte and fluid secretion in salivary acinar cells. *Am J Physiol* 263(6):G823–G837, <https://doi.org/0193-1857/92>
- Palk L., Sneyd J., Shuttleworth T. J., Yule D. I., Crampin E. J. (2010) A dynamic model of saliva secretion. *J Theor Biol* 266(4):625–640, <https://doi.org/10.1016/j.jtbi.2010.06.027>
- Palk L., Sneyd J., Patterson K., Shuttleworth T. J., Yule D. I., Maclarens O., Crampin E. J. (2012) Modelling the effects of calcium waves and oscillations on saliva secretion. *J Theor Biol* 305:45–53, <https://doi.org/10.1016/j.jtbi.2012.04.009>
- Peña-Münzenmayer G., Catalán M. A., Kondo Y., Jaramillo Y., Liu F., Shull G. E., Melvin J. E. (2015) Ae4 (Slc4a9) anion exchanger drives Cl^- uptake-dependent fluid secretion by mouse submandibular gland acinar cells. *J Biol Chem* 290(17):10,677–10,688, <https://doi.org/10.1074/jbc.M114.612895>
- Poulsen J., Bledsoe S. (1978) Salivary gland K^+ transport: in vivo studies with K^+ -specific microelectrodes. *Am J Physiol* 234(1):E79–E83, <https://doi.org/10.1152/ajpendo.1978.234.1.E79>
- Romanenko V. G., Catalán M. A., Brown D. A., Putzier I., Hartzell H. C., Marmorstein A. D., Gonzalez-Begne M., Rock J. R., Harfe B. D., Melvin J. E. (2010) Tmem16A encodes the Ca^{2+} -activated Cl^- channel in mouse submandibular salivary gland acinar cells. *J Biol Chem* 285(17):12,990–13,001, <https://doi.org/10.1074/jbc.M109.068544>
- Sigüenza E., A. Catalán M., Peña-Münzenmayer G., E. Melvin J., Sneyd J. (2018) A mathematical model supports a key role for ae4 (slc4a9) in salivary gland secretion. *Bull Math Biol* 80(2):255–282, <https://doi.org/10.1007/s11538-017-0370-6>
- Silva P., Stoff J., Field M., Fine L., Forrest J., Epstein F. (1977) Mechanism of active chloride secretion by shark rectal gland: role of Na-K-ATPase in chloride transport. *Am J Physiol* 233(4):F298–F306, <https://doi.org/10.1038/k1.1996.224>

- Soltoff S., McMillian M., Cantley L., Cragoe E., Talamo B. (1989) Effects of muscarinic, alpha-adrenergic, and substance P agonists and ionomycin on ion transport mechanisms in the rat parotid acinar cell. the dependence of ion transport on intracellular calcium. *J Gen Physiol* 93(2):285–319, <https://doi.org/10.1085/jgp.93.2.285>
- Swietach P., Zaniboni M., Stewart A. K., Rossini A., Spitzer K. W., Vaughan-Jones R. D. (2003) Modelling intracellular H⁺ ion diffusion. *Prog Biophys Mol Biol* 83(2):69–100
- Tanimura A. (2009) Mechanism of Calcium Waves and Oscillations in Non-Excitable Cells. *Int J Dent Oral-Med Sci* 8(1):1–11, <https://doi.org/10.5466/ijoms.8.1>
- Young J. A. (1968) Microperfusion investigation of chloride fluxes across the epithelium of the main excretory duct of the rat submaxillary gland. *Pflugers Archiv* 303(4):366–374